nature physics

SUPPLEMENTARY INFORMATION

DOI: 10.1038/NPHYS3201

Magnetic control of valley pseudospin in monolayer WSe_2

Grant Aivazian, Zhirui Gong, Aaron M. Jones, Rui-Lin Chu, Jiaqiang Yan, David G. Mandrus, Chuanwei Zhang, David Cobden, Wang Yao, and Xiaodong Xu

Supplementary Text

S1. Computing the valley Zeeman effect in multiple samples.

The peak splitting due to the valley Zeeman effect is small compared to the width of the photoluminescence (PL) peaks so care must be taken in determining the Zeeman splitting. The peaks are slightly asymmetric, with shape varying somewhat with magnetic field, and do not conform well to a Gaussian or Lorentzian peak shape. We use two methods to determine the peak position and hence the Zeeman splitting, both of which make no assumptions about the peak shape. As shown in Figure 1c, they agree very well. The first, "max point", simply finds the 15 points in each spectrum with the most counts and assigns the peak position to the median value of these points. This method is insensitive to the trion peak, which is too far away to influence these points; however, it is more sensitive to noise as it only considers a few points. The second method, "weighted average", computes the "center of mass" of the peak, $\int Ef(E)dE / \int f(E)dE$, where $f(E)$ is the PL spectral density and E is photon energy. In this method the effect of noise is greatly reduced because it makes use of all the several hundred points that make up the spectrum, but on the other hand it is more sensitive to the trion peak, which will tend to over-weight the low-energy side of the peak. However, since the valley exciton Zeeman splitting is small and we are interested in the difference between the σ+ and σ- peaks, the weak trion effects on both peaks tend to balance each other out. The data in Fig. 1c and Fig. S1a are from two different samples. We can see that the splitting as a function of magnetic field obtained by these two different methods has little difference.

Eight samples were measured and all were observed to have a splitting linear in the applied field. In Figure S1b we plot the fitted slope of the splittings from all the samples, in units of Bohr magnetons. The data presented in the main text is from the fifth sample. We see that the data can be split into two groups with mean values of 1.57 μ_B and 2.86 μ_B. The origin of this bimodal distribution in the g-factors is unclear due to the lack of understanding of what external factors can affect the g-factors in these new materials. Future studies will be necessary to quantitatively determine the effect of variables such as strain, doping, and substrate on the magnetic properties. However, all samples show similar behavior in their valley polarization as a function of the applied field (i.e., the "X" and "V" patterns).

DOI: 10.1038/NPHYS3201

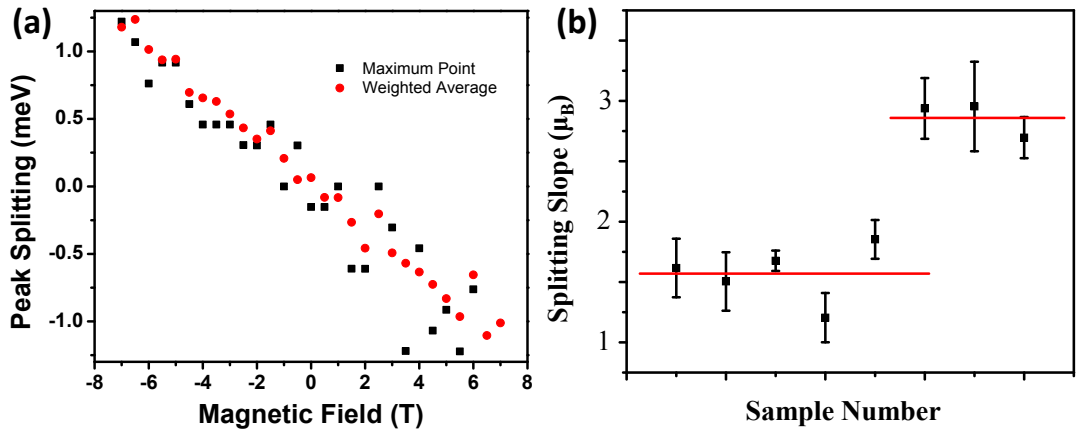

Supplementary Figure S1 | Statistics of valley Zeeman splitting. a) Splitting in another sample as a function of applied magnetic field. It also shows a linear splitting with similar results for both methods of peak extraction. b) Each point shows the slope of the Zeeman splitting for eight different samples measured. The fifth data point is from the sample presented in the main text. The samples appear to fall into two groups, for reasons presently unknown.

S2. Effective masses and valley magnetic moment: deviation from massive Dirac model

To leading order, the conduction and valence band edges are described by the massive Dirac fermion model and possess identical effective masses and valley magnetic moments [S1], which lead to identical Zeeman shifts of the conduction and valence bands. Thus for the Zeeman splitting of the valley exciton pseudospin, there would be no contributions from the valley magnetic moment. Nevertheless, deviations from the massive Dirac fermion model resulting from couplings to the higher energy bands will introduce a significant difference between the effective masses and valley magnetic moments of the electron and hole [S1, S2]. The difference between the valley magnetic moments of electron and hole can then contribute to the Zeeman splitting of valley exciton pseudospin.

We consider here the three-band tight-binding (TB) model with either nearest neighbor (NN)

	NN +GGA	NN + LDA	TNN +GGA	TNN +LDA
$m_e^*(m_0)$	0.417	0.424	0.388	0.380
$m_h^*(m_0)$	0.627	0.642	0.576	0.530
$\Delta\alpha$	0.246	0.235	1.071	1.221

Table S1 | Difference in the valley magnetic moments of electron and hole in monolayer WSe_2. The first two rows are the effective masses of electrons and holes, and the last role lists the difference in the valley g-factor of electrons and holes, calculated with the three-band tight-binding (TB) model with either nearest neighbor (NN) or third nearest neighbor (TNN) hopping, where the TB parameters are obtained by fitting first-principles (FP) band structures of relaxed monolayers of WSe2 in both generalized-gradient approximation (GGA) and local-density approximation (LDA) cases [S2].

or third nearest neighbor (TNN) hoppings [S2], where the TB parameters are obtained by fitting first-principles band structures of relaxed monolayers of WSe_2 in both generalized-gradient approximation (GGA) and local-density approximation (LDA) cases. This is the simplest model for going beyond the massive Dirac fermion description of the band edges in monolayer TMDs. The results for the effective masses and the difference in the valley magnetic moments of electrons and holes are listed in Table S1. The magnetic moment is calculated with the multi-band formula in Ref. S1. We note that the NN and TNN models with parameters fitted from different first-principle band structure calculations lead to different values of valley magnetic moments, suggesting that the models are oversimplified for quantitative description of such quantity. They are quoted here simply to illustrate the variety of the magnetic moments of electrons and holes that are obtained from calculations when one goes beyond the massive Dirac fermion model. We note that within this three-band model, apparently the sign of $\Delta\alpha$ is correlated with the sign of effective mass difference between hole and electron. However, for multi-band models in general, we are not certain whether the two signs are connected. The fact that $\Delta\alpha$ is nonzero, meaning that the electron and hole valley magnetic moments differ, does nevertheless imply that these particles no longer exactly comply with the simple massive Dirac fermion model.

S3. Exciton dispersion in magnetic field and exciton formations

In monolayer TMDs, the intervalley electron-hole exchange interaction strongly couples the valley pseudospin of an exciton to its center-of-mass motion [S3]. The Hamiltonian of the valley exciton is:

$$H = \hbar\omega_0 + \frac{\hbar^2 k^2}{2M_0} + V'(k) + \tau_+ V_{inter}(\boldsymbol{k}) + \tau_- V^*_{inter}(\boldsymbol{k}),$$

where $V_{inter}(\boldsymbol{k}) = V(k)e^{-2i\theta}$ is from the inter-valley electron-hole exchange, $\mathbf{k} \equiv (k_x, k_y) = (k\cos\theta, k\sin\theta)$ being the center-of-mass wavevector and $\boldsymbol{\tau}$ the Pauli matrix describing the exciton valley pseudospin. The pseudospin-independent term $V'(k)$ is due to the intravalley electron-hole exchange. M_0 is the exciton mass, $\hbar\omega_0 \sim 1.75$ eV is the exciton energy at $\mathbf{k} = 0$, and K is the distance from K to Γ point in the first Brillouin zone.

Because of the exceptionally strong Coulomb binding of excitons in monolayer TMDs, the electron-hole exchange is also strong, so the exciton dispersion splits into two well separated branches by the intervalley exchange. On the boundary of the light cone, the splitting between the two branches is estimated to be ~ meV. If considering the unscreened Coulomb interaction in 2D, $V(k)$ and $V'(k)$ both have linear dependence in k, however screening will change the dependence to quadratic. These details are not important for our discussions. The key factor here is that the upper branch has a much steeper dispersion compared to the lower branch: at the same energy, states in the lower branch correspond to much larger exciton momentum, compared to those in the upper branch, so that the exciton scatterings in the upper branch require much smaller momentum change.

At finite magnetic field applied in the perpendicular direction, the excitonic valley pseudospin spin is subject to an effective Zeeman field $-\tau_z\Delta(B)/2$, where $\Delta(B) = 2(2 - \Delta\alpha)\mu_B B$ as discussed in the main text. This Zeeman field opens a finite gap at the k=0 point, giving rise to the two-branch exciton dispersion as shown in supplementary Figure S2. In the k-space region with $V(k) \ll \Delta(B)$, the exciton eigenstates are polarized in one of the valleys (denoted by the red and blue colors respectively in Fig. S2) and coupled to circularly polarized

DOI: 10.1038/NPHYS3201

photons. When the magnetic field changes sign, the circular polarizations of the upper and lower branches switch. In the k-space region with $V(k) \gg \Delta(B)$ excitons are linearly polarized (denoted by the green and purple colors in Fig. S2) and are not affected by the magnetic field. Only those states within the light cone can emit photons.

In the photoluminescence measurement, the excitation laser has a frequency well above ω_0. Below we analyze the efficiency of bright exciton formation following the excitation by circularly polarized laser. Consider first a positive magnetic field (Figs. 3b and c, main text). The center of the upper exciton branch is then σ^- polarized, and the center of the lower exciton branch is σ^+ polarized. Under excitation by σ^-, excitons can form at the center of the upper branch through the valley-conserving formation channel with rate γ_1, and at the center of the lower branch through the valley-flipping channel with rate γ_2. We note that the valley-flipping exciton formation process concerns only the intervalley scattering that occurs before the ground state exciton is formed. The scattering between the valley configurations of ground state exciton is modeled by a separate rate r_1. The valley-conserving rate is more efficient than the valley-flipping one, i.e. $\gamma_1 > \gamma_2$ as evidenced by the fact that exciton PL always has the same circular polarization with the excitation laser.

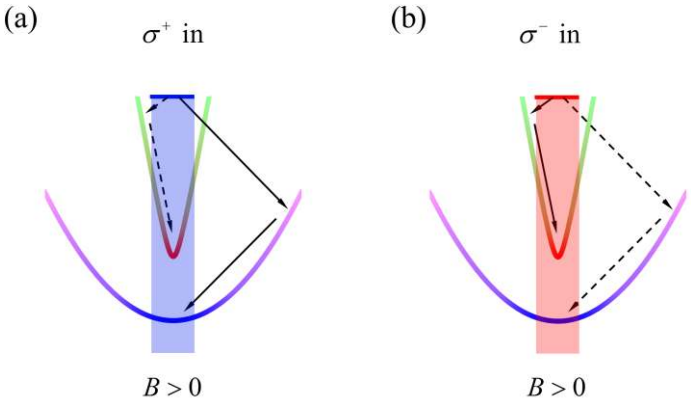

Supplementary Figure S2 | Schematic of the exciton formation processes. The shaded region denotes the light cone, and blue and red colors denote the (a) σ^+ or (b) σ^- excitation respectively. The purple and green colors on the dispersion curves denote respectively linear polarization transverse or longitudinal to the momentum. For $B > 0$, comparing the valley-conserving exciton formation processes (solid arrows), the one under σ^- excitation is facilitated in the upper exciton branch by its steeper dispersion, and is therefore more efficient than the one under σ^+ excitation which requires larger momentum transfers by scattering in the lower branch to reach the light cone. Similarly, comparing the valley-flipping exciton formations (dashed arrows), the one under σ^+ excitation is more efficient than that under σ^- excitation.

Now we compare with the σ^+ excitation under positive magnetic field. The valley-conserving exciton formation is then at the center of the lower branch, while the valley-flipping formation is at the center of the upper branch. This can result in a difference between $\gamma_1(\sigma^+, B > 0)$ and $\gamma_1(\sigma^-, B > 0)$, denoting, respectively, the valley-conserving exciton formation rate under σ^+ and σ- excitations. This is because the upper and lower exciton branches have different dispersions. The valley-conserving exciton formation under σ^- excitation (solid arrows, Fig. S2b) is facilitated in the upper exciton branch by its steeper dispersion, and is therefore more efficient than the valley-conserving exciton formation under σ^+ excitation (solid arrows, Fig. S2a) which requires larger momentum transfers by scattering in the lower branch to reach the light cone. Thus, we expect $\gamma_1(\sigma^+, B > 0) < \gamma_1(\sigma^-, B > 0)$. Similarly, comparing the valley-flipping exciton formations (dashed arrows in Fig. S2), the one

under σ^+ excitation is more efficient than that under σ^- excitation, i.e. $\gamma_2(\sigma^+, B > 0) > \gamma_2(\sigma^-, B > 0)$. Therefore, one may expect that $\frac{\gamma_1(\sigma^+,B>0)}{\gamma_2(\sigma^+,B>0)} < \frac{\gamma_1(B=0)}{\gamma_2(B=0)} < \frac{\gamma_1(\sigma^-,B>0)}{\gamma_2(\sigma^-,B>0)}$. The analysis is similar when the magnetic field is negative. This can qualitatively explain the X-pattern observed for the PL polarization.

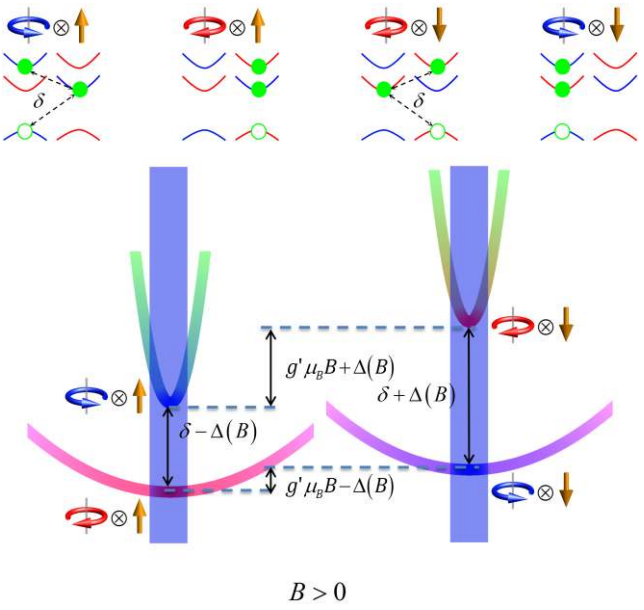

Supplementary Figure S3: Top: four configurations of X- labeled by the polarization of photon emission and the spin orientation of the extra electron. Bottom: X- dispersion under positive magnetic field. Left (right) is the dispersion of trion with the excess electron in the spin up state in –K (spin down state in K).

S4. Magnetic field effects on negative trion

Negatively charged trions (X^-) are formed when an electron-hole pair binds an excess electron. Assuming the excess electron is in the lowest energy conduction band, X^- has four ground state configurations as shown in supplementary Figure S3 (top row). These four configurations can be put into two groups according to the spin configuration of the excess electron (i.e. spin down in valley K, and spin up in valley –K). The electron-hole exchange interaction couples the two configurations in each group. Hence X^- has two sets of valley-orbit coupled bands with the excess electron in a spin up state (at valley K) and spin down state (at –K) respectively (see Figure S3). We also need to take into account the additional exchange energy between the excess electron and the recombining electron-hole pair, which is finite for the first and third configurations shown in Figure S3 (top row), but zero for the second and fourth configurations where the spin of the excess electron is orthogonal to the other two particles. This exchange coupling is then effectively a Zeeman field in the z-direction with sign conditioned on the spin of excess electron [S3]. This opens up a gap $\delta \sim 6$ meV at zero magnetic field at k=0, where the sign of the gap depends on the spin of the excess electron (Fig. S3 bottom).

In finite magnetic field, the trion Hamiltonian is then given by

$$H_- = \hbar\omega_- + \frac{\hbar^2 k^2}{2M_-} + V'(k) + \tau_+ V_{inter}(\boldsymbol{k}) + \tau_- V^*_{inter}(\boldsymbol{k}) - \frac{\Delta(B)}{2}\tau_z - \frac{\delta}{2}\tau_z s_z + \frac{g'\mu_B B}{2} s_z \qquad (1)$$

The fourth and fifth terms are the valley-orbit coupling by the intervalley electron-hole exchange, the six term is the Zeeman splitting by the magnetic field, the seventh term is the gap opened by the exchange interaction with the excess electron, and the last term is the Zeeman energy of the excess electron in the magnetic field with $g' = 2(\alpha_e - 1)$. We note that $\Delta(B) \ll \delta$ over the entire range of magnetic field in the experiment. Therefore, unlike the neutral exciton, the trion dispersions are not much affected by the magnetic field, except for the relative shift between the two sets of dispersions with the excess electron on spin up and down states respectively (see supplementary Fig. S3 bottom).

S5. Rate equations for modeling the exciton PL polarization

DOI: 10.1038/NPHYS3201

Here we model the formation and valley-relaxation processes of neutral exciton and negatively charged trion with rate equations. As shown by the level scheme in Fig. 3b, under σ^+ excitation and positive magnetic field, the exciton formation and recombination processes are described by the following rate equations:

$$\begin{cases} \frac{d}{dt}N_+ = \gamma_1 - \Gamma N_+ - r_1 N_+ + r_1{}' N_- \\ \frac{d}{dt}N_- = \gamma_2 - \Gamma N_- + r_1 N_+ - r_1{}' N_- \end{cases}, \qquad (2)$$

where $N_\pm$ are the populations of the bright excitons in valley +K and –K within the light cone, and γ_1 and γ_2 are their corresponding formation rates (i.e. the valley-conserving and valley-flip ones, c.f. supplementary note S3). Γ is the exciton recombination rate. $r_1{}'$ (r_1) is the relaxation rate from the higher (lower) energy valley configuration to the lower (higher) energy one in the magnetic field, and we therefore expect $r_1' \geq r_1$. So when magnetic field flips sign, $r_1{}'$ and r_1 shall be switched in Eq. (2). γ_1 and γ_2 are the valley-conserving and valley-flip exciton formation rates respectively as shown in Fig. 3b. The rate equation under σ^- excitation is similar but with γ_1 and γ_2 switched, since the valley conserving channel now leads to formation of exciton at –K (with population N_-). The degree of PL polarization is given by $P_\sigma \equiv \frac{\sigma(N_+ - N_-)}{(N_+ + N_-)}$, ($\sigma = \pm 1$ for $\sigma^\pm$ excitation), where positive value means the PL has the same polarization as that of the excitation.

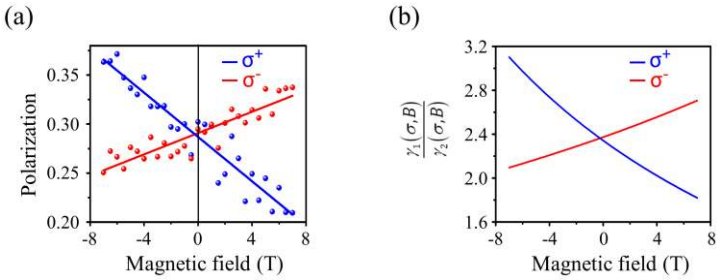

Supplementary Figure S4: (a) The dots are the measured polarization of the photoluminescence from exciton under σ^+ (blue) and σ^- (red) excitation. The blue and red lines are the polarizations calculated with our model (Eq. (3)), by assuming the ratio $\gamma_1(\sigma, B)/\gamma_2(\sigma, B)$ as shown in part (b). Other parameters: $r_1 = r_1' = 0.2\Gamma$.

From the steady-state solution of Eq. (2), we find

$$P_\sigma = \frac{\Gamma}{\Gamma + r_1{}' + r_1} \times \frac{\gamma_1 - \gamma_2}{\gamma_1 + \gamma_2} + \sigma \frac{B}{|B|} \frac{(r_1{}' - r_1)}{\Gamma + r_1{}' + r_1}. \qquad (3)$$

In the first term of the above equation, the factor $(\gamma_1 - \gamma_2)/(\gamma_1 + \gamma_2)$ corresponds to the valley depolarization in the exciton formation process. As discussed in the supplementary note S3, $\frac{\gamma_1(\sigma^+, B>0)}{\gamma_2(\sigma^+, B>0)} < \frac{\gamma_1(B=0)}{\gamma_2(B=0)} < \frac{\gamma_1(\sigma^-, B>0)}{\gamma_2(\sigma^-, B>0)}$, and this magnetic field dependences of γ_1 and γ_2 can indeed give rise to the observed X pattern. The second term is proportional to the difference between $r_1{}'$ and r_1, which also corresponds to a X-pattern, but opposite to the one observed. This suggests that it has a small contribution in the experiment, i.e. $r_1' - r_1 \ll \Gamma$. In supplementary Figure S4, we show that with a reasonable choice of parameters, the observed X-pattern can be fitted quantitatively well. We note that if the system has time reversal symmetry in the absence of magnetic field and optical pump, then we shall expect the relation $\frac{\gamma_1(\sigma^+, B)}{\gamma_2(\sigma^+, B)} = \frac{\gamma_1(\sigma^-, -B)}{\gamma_2(\sigma^-, -B)}$, and the observed X-pattern shall be symmetric. The fact that the X pattern is asymmetric could

imply that there is time reversal symmetry breaking.

S6. Rate equations for modeling the trion PL polarization

Next we turn to the negatively charged trion (X^-). As illustrated by the level scheme in supplementary Figure S5, the trion formation and recombination processes are described by the following rate equations:

$$\begin{cases} \frac{d}{dt}N_+^l = \rho_\uparrow\gamma_1 - \Gamma N_+^l - r_1 N_+^l + r_1 N_-^l - r_2(\Delta_+)N_+^l + r_2'(\Delta_+)N_-^r \\ \frac{d}{dt}N_-^l = \rho_\uparrow\gamma_2 - \Gamma N_-^l + r_1 N_+^l - r_1 N_-^l - r_2(\Delta_-)N_-^l + r_2'(\Delta_-)N_+^r \\ \frac{d}{dt}N_+^r = \rho_\downarrow\gamma_1 - \Gamma N_+^r - r_1 N_+^r + r_1 N_-^r + r_2(\Delta_-)N_-^l - r_2'(\Delta_-)N_+^r \\ \frac{d}{dt}N_-^r = \rho_\downarrow\gamma_2 - \Gamma N_-^r + r_1 N_+^r - r_1 N_-^r + r_2(\Delta_+)N_+^l - r_2'(\Delta_+)N_-^r \end{cases}, \quad (4)$$

where the superscript l and r represent the left and right set of energy dispersion with the excess electron on spin up and down state respectively (c.f. supplementary Fig. S5). Similar to the exciton case, γ_1 and γ_2 are the valley-conserving and valley-flip trion formation rates, which depends on the sign and size of the gap at k=0. However, since the exchange induced gap is much larger than the Zeeman shift in the magnetic field ($\delta \gg \Delta(B)$), the field has negligible effect on γ_1 and γ_2.

$\rho_\uparrow$ and $\rho_\downarrow$ in Eq. (4) are the portion of the spin up and spin down carriers in the electron gas in the steady state, which depends on the magnetic field B as well as the polarization σ of the excitation light, since the circularly polarized light effectively pumps electron spin polarization. $\varsigma(\sigma, B) = \frac{\rho_\uparrow - \rho_\downarrow}{\rho_\uparrow + \rho_\downarrow}$ is then the steady-state spin polarization of the electron gas and it determines the partition of the pumping rates of the two groups of trion (i.e. with excess electron in the spin up and down states respectively).

r_2' and r_2 here denote the relaxations between the two groups of trion as shown in Fig. 3e and supplementary Figure S5. r_2' (r_2) is the relaxation rate from the higher (lower) energy state to the lower (higher) energy one in the magnetic field, which in general depends on the energy splitting Δ.

The straightforward calculation gives the degree of PL polarization as

$$P_\sigma = V_1(\sigma, B) + V_2(\sigma, B) + X_1(\sigma, B) + X_2(\sigma, B) \quad (5)$$

where

$$V_1(\sigma, B) = P_0 \frac{\Gamma + 2r_1}{2r_1} \frac{r_1[1/R(\Delta_+) + 1/R(\Delta_-)]}{r_1[1/R(\Delta_+) + 1/R(\Delta_-)] + 1} \quad (6)$$

$$V_2(\sigma, B) = \varsigma(\sigma, B) P_0 \frac{B}{2|B|} \frac{r(\Delta_+)/R(\Delta_+) + r(\Delta_-)/R(\Delta_-)}{r_1[1/R(\Delta_+) + 1/R(\Delta_-)] + 1}, \quad (7)$$

$$X_1(\sigma, B) = \sigma\varsigma(\sigma, B) \frac{1}{2} \frac{\Gamma[1/R(\Delta_+) - 1/R(\Delta_-)]}{r_1[1/R(\Delta_+) + 1/R(\Delta_-)] + 1}, \quad (8)$$

$$X_2(\sigma, B) = \sigma \frac{B}{2|B|} \frac{r(\Delta_+)/R(\Delta_+) - r(\Delta_-)/R(\Delta_-)}{r_1[1/R(\Delta_+) + 1/R(\Delta_-)] + 1} \quad (9)$$

$\sigma = \pm 1$ for $\sigma^\pm$ excitation. In the above equations, we have defined $P_0 \equiv \frac{\Gamma}{\Gamma + 2r_1} \frac{\gamma_1 - \gamma_2}{\gamma_1 + \gamma_2}$, $R(\Delta) \equiv \Gamma + r_2'(\Delta) + r_2(\Delta)$ and $r(\Delta) \equiv r_2'(\Delta) - r_2(\Delta)$.

DOI: 10.1038/NPHYS3201

If the magnetic field induced splitting Δ_+ and Δ_- quenches the relaxation between the two group of trions (c.f. Fig. S5), $R(\Delta)$ decreases with the increase in the magnetic field strength. Then the term $V_1(\sigma, B)$ corresponds to a V-pattern of the PL polarization, where $V_1(\sigma, B = 0) = P_0 \frac{\Gamma+2r_1}{R(\Delta=0)+2r_1}$, which agrees with the main feature of the observed PL polarization in the experiments (see supplementary Figure S6). The term X_1 vanishes at $B = 0$, and at finite field it depends on $\varsigma(\sigma, B)$, which relies on the detail of the optical spin pumping and the spin relaxation. Nevertheless, some qualitative behaviors can be determined. First, time reversal symmetry requires $-\varsigma(\sigma, B) = \varsigma(-\sigma, -B)$. Second, for $B > 0$, optical pumping by σ^- (σ^+) excitation tends to pump spin to the low (high) energy state in the magnetic field, so the spin polarization is higher (lower), i.e. $\varsigma(\sigma^+, B > 0) \leq \varsigma(\sigma^-, B > 0)$. Therefore X_1 corresponds to a X-like pattern, which can account for the difference between the V-pattern of PL polarization under σ^+ and σ^- excitations (c.f. blue and red data points in Fig. S6 (a)).

For the other two contributions to the PL polarization, $X_2(\sigma, B)$ is also a X-like pattern, and $V_2(\sigma, B)$ is a V-like pattern. We note that $r(\Delta) \ll R(\Delta)$ is expected in the entire range of magnetic field considered. Thus $V_2(\sigma, B)$ and $X_2(\sigma, B)$ can be dropped as they are much smaller compared to $V_1(\sigma, B)$ and $X_1(\sigma, B)$ respectively.

In supplementary Figure S6, we show that with a reasonable choice of parameters, the observed V-pattern can be fitted quantitatively well.

S7. Hanle effect

An exciton with in-plane valley pseudospin is defined as a linear superposition of +K and –K excitons. Since +K and -K excitons couple to $\sigma+$ and $\sigma-$ photons respectively, an exciton with in-plane valley pseudospin couples to linearly polarized photon and therefore can be generated by linearly polarized excitation. The perpendicular magnetic field lifts the energy degeneracy between +K and -K excitons through the Zeeman splitting $-\tau_z\Delta(B)/2$ along the z-direction. Therefore, the in-plane pseudospin will precess about the perpendicular magnetic field with Larmor frequency $\Delta(B)/\hbar$, which gives rise to the Hanle effect. In contrast, the band-edge electron or hole spin does not show a Hanle effect in perpendicular magnetic field, because the spin up and down states are in different valleys which can not be coupled by magnetic field. One therefore cannot have an in-plane spin precession of an individual electron (or hole) about the perpendicular magnetic field, although the precession of excitonic valley pseudospin is allowed.

Here we lack detailed information about the timescale of the exciton formation process, so the effects of valley pseudospin precession and decoherence during the formation process cannot be accurately determined.

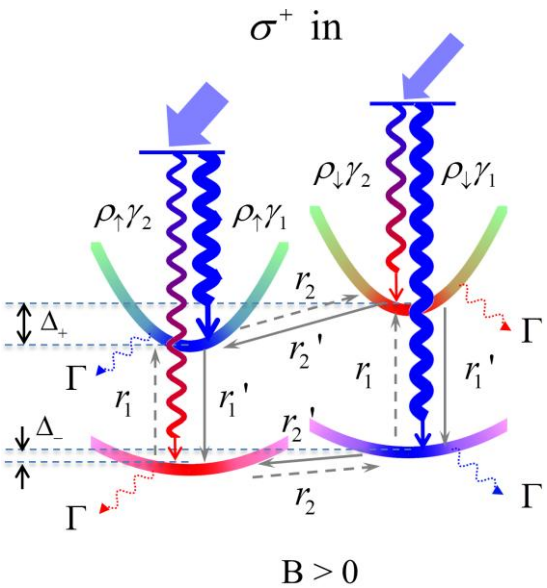

Supplementary Figure S5: Simplified level scheme for the exciton formation and valley relaxation dynamics of trion. See text in S6 for details.

If we *neglect* the magnetic field effect in the exciton formation process, then the equation of motion for the valley pseudospin vector $\boldsymbol{\tau}$ of the exciton ground state is:

$$\frac{\mathbf{d\tau}}{\boldsymbol{dt}} = -\frac{\Delta(B)}{\hbar} \times \boldsymbol{\tau} - (\Gamma^d + \Gamma)\boldsymbol{\tau} + \Gamma\boldsymbol{\tau}_0. \qquad (10)$$

The first term on the right hand side describes the pseudospin precession in the effective magnetic field. In the second term, Γ^d is the valley decoherence rate, and Γ the exciton recombination rate. The last term describes the pumping of exciton ground state population by the linear (x) polarized excitation. $\boldsymbol{\tau}_0 = (\tau_0, 0, 0)$ corresponds to the steady-state exciton valley polarization in the limit of zero Γ^d and $\Delta(B)$, and τ_0 is determined by the exciton formation process. The steady state solution of Eq. (10) is then: $\tau_x = \tau_0 \frac{\hbar^2\Gamma\Gamma^*}{(\hbar\Gamma^*)^2+(\Delta(\mathrm{B}))^2}$, $\Gamma^* \equiv \Gamma + \Gamma^d$. We note that exciton with valley pseudospin along +x (-x) direction emits photon linearly polarized in x (y). So the linear polarization of the exciton PL is $\mathrm{P} = |\tau_x| = \frac{\mathrm{P}_0}{1+(\Delta(\mathrm{B})/\hbar\Gamma^*)^2}$, $P_0 = \tau_0\Gamma/\Gamma^*$ being the PL polarization at zero magnetic field. Because of the precession of the valley pseudospin, its time-averaged projection along the x-direction is suppressed, and hence the linear polarization of the exciton PL is quenched, which is the well-known Hanle effect [S4]. The half-width of the Hanle peak then corresponds to the decay rate Γ^*. Fitting the data in Fig.

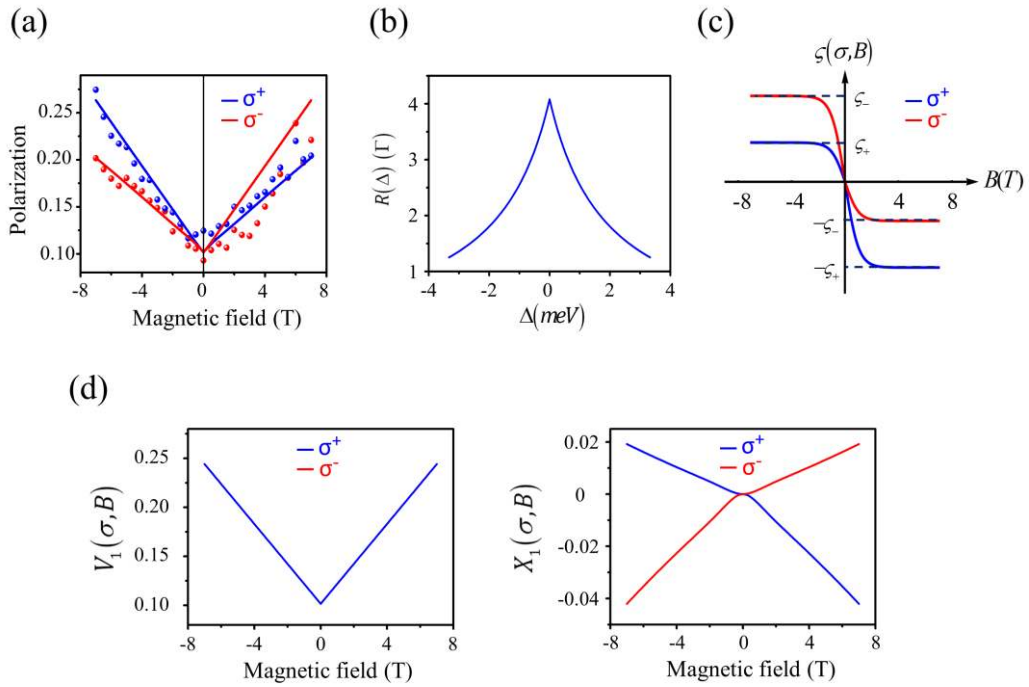

Supplementary Figure S6: (a) The dots are the measured polarization of photoluminescence from trion under σ^+ (blue) and σ^- (red) excitation. The blue and red curves are the PL polarizations calculated with our model (Eq. (5-9) in supplementary note S6), by assuming $\mathrm{R}(\Delta)$ and $\varsigma(\sigma, \mathrm{B})$ as shown in (b) and (c) respectively. Other parameters in the calculation: $\mathrm{r}_1 = \mathrm{r}_1' = 0.2\Gamma, \varsigma_+ = 0.46, \varsigma_- = 0.21, \alpha_e = 4.33$ and $\alpha_h = 3.10$. (d) The contributions from terms $V_1(\sigma, B)$ and $X_1(\sigma, B)$ respectively (c.f. Eq. (5), (6), (8) in supplementary note S6).

DOI: 10.1038/NPHYS3201

4(b) yields $\Gamma^* \approx 1.5$ THz, and $\Gamma \approx 0.5\tau_0^{-1}$ THz.

The above analysis *neglecting* the magnetic field effect in the exciton formation process leads to the exciton recombination lifetime and exciton valley dephasing time both of picosecond timescale, which are significantly shorter than their values obtained by time-resolved measurements [S5]. This in turn suggests that the magnetic field effect in the exciton formation process is crucial in determining the measured field dependence of linear polarization.

S8. Additional data exhibiting the "X" and "V" patterns

In supplementary Figure S7 we plot the polarization as a function of applied magnetic field for a sample with large Zeeman splitting (sample 6 in Fig S1b). This shows the same "X" and "V" patterns as for the sample in Figs. 2e-f of the main text, proving that the result is robust.

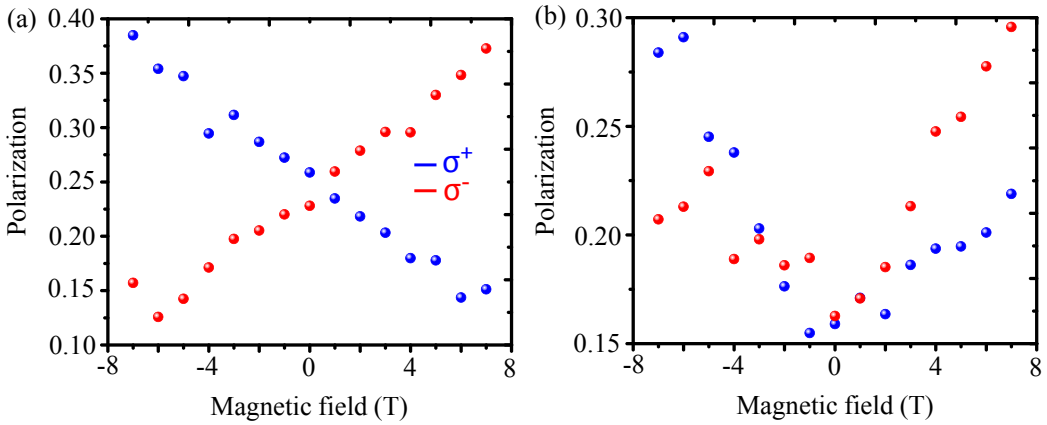

Supplementary Figure S7: Valley polarization as a function of magnetic field for both neutral exciton (a) and trion (b) for a different sample to that used for Figs. 2e-f in the main text.

Supplementary References

[S1] Wang Yao, Di Xiao, and Qian Niu, Valley-dependent optoelectronics from inversion symmetry breaking, Phys. Rev. B **77**, 235406 (2008).

[S2] Gui-Bin Liu, Wen-Yu Shan, Yugui Yao, Wang Yao, and Di Xiao, Three-band tight-binding model for monolayers of group-VIB transition metal dichalcogenides, Phys. Rev. B **88**, 085433 (2013).

[S3] Hongyi Yu, Guibin Liu, Pu Gong, Xiaodong Xu, and Wang Yao, Bright excitons in monolayer transition metal dichalcogenides: from Dirac cones to Dirac saddle points, Nature Communications **5**, 3876 (2014).

[S4] Michel I. Dyakonov, Spin Physics in Semiconductors-Springer Series in Solid-State Sciences Volume 157, pp 21-22, Springer (2008).

[S5] Wang, G., Marie, X., Gerber, I., Amand, T., Lagarde, D., Bouet, L., Vidal, M., Balocchi, A. & Urbaszek, B. Non-linear Optical Spectroscopy of Excited Exciton States for Efficient Valley Coherence Generation in WSe2 Monolayers, arXiv:1404.0056 (2014).